Chapter 8

Full Field Optical Coherence Microscopy: Imaging and Image Processing for Micro-Material Research Applications

Bettina Heise, Stefan Schausberger and David Stifter

Additional information is available at the end of the chapter

http://dx.doi.org/10.5772/53509

1. Introduction

Non-destructive optical imaging and probing techniques have found entrance and success in material sciences favoured by their non-invasive investigation character. X-ray computer tomography (CT) applied in a different size scale (e.g. as micro-CT and nano-CT [1]) is well established as a non-destructive technique in the field of material inspection. CT imaging delivers highly contrasted images of the internal of the specimens. It includes information about inclusions or cavities, and about the size and distribution of particles and pores within the technical material. Furthermore, ultrasound and acousto-optic imaging may also provide valuable insights into internal cracks and flaws, density or concentration variations, or even features as material elasticity. Although both techniques are versatile for use in different applications in material analysis, they also show restrictions: for biological samples in particular, there are the hazards of X-ray radiation; the techniques obey typical resolution limits in relation to the sample dimensions, or they require an additional coupling medium as in ultrasonic imaging (US).

With the availability of powerful broadband near infrared wavelength (NIR) light sources some decades ago, low-coherence interferometry (LCI) for the investigation of scattering or semi-transparent materials has become an alternative to CT and US methods. In 1991, optical coherence tomography (OCT) was introduced as an imaging technique by [2]. At the beginning, OCT mainly gained ground in the field of medical diagnostics, in particular in ophthalmology, representing a novel visualization technique for different ocular diseases, followed by numerous applications in cardiology, dentistry, dermatology, nephrology, amongst others

[3-6]. The imaging capabilities of OCT for subcutaneous assessment of the specimen need particular mention, and in the case of OCT being realized endoscopically [7], OCT can deliver valuable tissue information from various internal positions and sites within the human body.

The capability and specific use of OCT for non-medical purposes as in material sciences or arts has been recognized relatively late, arising with metrology and topographic profiling of microelectronic circuits [8] and optical components (which rather resembles optical time domain reflectometry (ODTR) or white light profilometry). The optical inspection of glass fibers and ceramic parts need to be mentioned, as well as further applications in art conservation (providing information about the conservation state of paintings [9] or about cracks and defects in porcelain and jade stones [10]), in paper inspection [11], or in dynamic process monitoring [12]. Recently, the use of OCT technique for the characterization of internal structures in polymer and compound materials such as multilayer foils, fiber-epoxy composites, or different types of extruded plastics and foams have become a research focus in polymer sciences [13].

Intensity-based OCT provides structural information about the probed specimen. The conventional modality can be modified by different polarization- or phase-sensitive functional extensions (naming e.g. polarization-sensitive OCT (PS-OCT), differential phase contrast OCT (DPC-OCT), or Doppler OCT), where also birefringence, phase or frequency can be extracted locally and in a depth–resolved way. Thereby additionally information about the specimen's functional behaviour (as optical anisotropies, elasticity, internal strain-stress distributions, or internal flow fields) can be gained [14, 15].

Recently reported OCT trends focus on various aspects. These trends are governed by the aim:

- to speed up the image acquisition time by ultra-fast scanning setups, working in Fourier domain and using special swept laser sources [16],
- to miniaturize the setup by using integrated optical techniques [17],
- to apply multi-modal imaging techniques and combining OCT with other imaging methods like fluorescence microscopy and spectroscopy [18] or hyper-spectral imaging techniques [19],
- to exploit non-linear effects in the signal like second harmonic generation or multi-photon imaging [20, 21],
- to work under a full-field imaging regime (instead of raster scanning techniques, as is typical for conventional OCT imaging) and in combination with microscopic elements to lead to so-called full-field optical coherence microscopy (FF-OCM) or full field OCT (FF-OCT) [22],
- to be supplemented by sophisticated image processing [23] or data analysis on graphics processing units (GPU) [24].

In this book chapter, we discuss the last two points in particular: First, full-field optical coherent microscopy -- its physical principles, similarities and differences to comparable OCT applications, its use for material characterization and dynamical inspections, and possible contrast modifications. Secondly, we discuss the enrichment of FF-OCM imaging by some illustrative

http://dx.doi.org/10.5772/53509

examples for image processing, showing the potential given by different mathematical algorithms in the field of object analysis.

2. FF-OCM imaging techniques

2.1. Physical principle

OCT and OCM imaging techniques are based on the principle of low-coherence interferometry. Both methods exploit the (low) coherence properties of broadband light sources, allowing for tuneable depth positioning of the narrow coherence gate/range within the sample. But whereas OCT (working in time- or frequency domain) represents a raster scanning technique probing along the beam line and sensing the reflected light point by point, FF-OCM produces interferometric images parallel to the sample surface. The entire field of view at the sample is illuminated at once by a low-coherent light beam, and the reflected light from an extended lateral region is received by a CCD or CMOS camera as detectors.

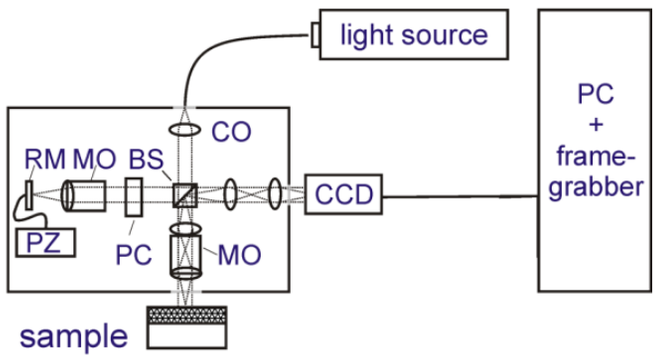

Figure 1. Scheme of the optical setup of the (time domain) FF-OCM realized in a Michelson/Linnik interferometer configuration, (BS: beamsplitter, CO: collimator, PC: path compensation, MO: microscopic objectives, RM: reference mirror, PZ: piezo translator).

In general, a FF-OCM setup is established in a Michelson/Linnik interferometric configuration (or for special purposes in some modifications as in Mach-Zehnder configuration), as depicted in Figure 1, with two identical optical elements assemblies (i.e. using the same micro-objectives and dispersion compensations) for both the sample and the reference arm. Applying broadband light sources for illumination and guaranteeing a homogeneously illuminated area, the incoming wave field is divided into sample and reference wave field. Both wave fields are reflected either by the sample or the reference mirror and superposed at the detector.

Interference can only occur when the optical path length of sample and reference arm are nearly identical with respect to the coherence length of the source. Then interferometric fringe images can be recorded within the coherence gate whose width is determined by the (temporal) coherence length of the source. The ratio of optical path length of sample to reference arm may be continuously changed by altering the position of the sample mounted at an axial motorized

translation stage. The reference mirror is placed on an oscillating piezoelectric translation stage (PZT). The PZT is driven either by a sinusoidal or by a saw tooth periodic oscillation. By displacing the reference mirror, a shift of the optical path length in fractions of the wavelength is introduced in a discrete or continuous way. It allows the recording of several phase shifted interferometric fringe images. By mathematical combination of the mutual phase-shifted images the FF-OCM reflectivity image can be obtained by a subsequent demodulation.

2.2. Light sources and resolution aspects

The choice of light source is of crucial importance for the penetration depth and the resolution achieved. It should be considered with respect to the planned application.

Similar to OCT, the axial resolution in FF-OCM is determined by the temporal coherence length of the source, which is proportional to the ratio $\lambda^2/\Delta\lambda$, with the wavelength λ and the spectral width $\Delta\lambda$ of the applied light source. The lateral resolution is mainly characterized by the numerical aperture (NA) of the objectives similar to conventional microscopy: high NA objectives increase lateral resolution. But high NA may also become dominant for axial resolution in FF-OCM [25], as the depth of field becomes very narrow for higher NA objectives. By careful dynamic focusing coherence gate and focus position of objectives can be matched within the investigated material.

As the penetration depth increases with the wavelength λ, light sources in the NIR range with a central wavelength of 1000 -- 1500 nm are often to be preferred to light sources at 800 nm, particularly for imaging technical structures, where water absorption does not play any role. However, axial resolution is reduced with increasing wavelength. Furthermore, the camera detection system also has to be adapted to the requested wavelength range using InGaAs-based detector types, which may cause higher financial costs.

For the light source itself, super-luminescence diodes [26], femto-second (fs) pulse laser [27], diode laser pumped super-continuum sources [28, 29], or thermal light sources [30] have been described in different illumination concepts, each with their advantages and drawbacks. Thermal light sources best prevent speckle noise and are not hampered by side-lobes as in the case of fs-laser or SLD. However, the adjustment of the setup is challenging. Halogen flash light sources are used for stroboscopic imaging and obtain an axial resolution less than 1 μm. A sophisticatedly tuned image acquisition scheme is required therefore. Broadband fs-pulse lasers with high repetition rates in the range of hundred MHz are another alternative for high resolution imaging; however these lasers are expensive. The use of nano-second pulse lasers is suggested in [31] as a valuable compromise: they achieve reasonable repetition rates while reducing costs.

In summary, the factors of resolution, penetration and costs must be weighed against each other when determining which light source to use in investigating technical materials or biological samples.

http://dx.doi.org/10.5772/53509

3. Demodulation

In interferometric imaging, an interference fringe pattern $I(x,y)$ can be described as

$$I(x,y) = B(x,y) + A(x,y)\cos(\phi(x,y)), \tag{1}$$

where $A(x,y)$ represents the amplitude modulation, φ(x,y) the phase modulation, and $B(x,y)$ is determined by any background illumination or surface characteristics.

Introducing multiple phase shifts $\varphi_n(x,y)$ between the different frames, a sequence $I_n(x,y)$ of interferometric images at a fixed depth position z may be described as

$$I_n(x,y) = B(x,y) + A(x,y)\cos(\phi(x,y) + \Delta\phi_n). \tag{2}$$

The aim of demodulation is to decode the amplitude (or phase) modulation, thereby extracting the interference fringe envelope at each lateral position. The amplitude modulation $A(x,y)$ is characterized by the local reflectivity of the sample at each depth position z (similar to OCT), and so the reflectivity map can be obtained by amplitude demodulation. It should be mentioned here that the phase/frequency modulation $\varphi(x,y)$ of the fringe pattern can also be exploited. It reveals details about local deformations of structures in the sub-wavelength range or about minimal refractive index changes in the imaged sample. However, reliable phase information can only be extracted from regions where sufficient amplitude modulation is guaranteed.

Different phase stepping approaches are used for data acquisition and demodulation. Generally, a set of phase-shifted interferometric fringe images (usually 4---8 frames) are recorded at each axial position of the sample. Assuming an equidistant sampling over the mirror oscillation, the amplitude and phase map can be obtained by a complex addition of the shifted interference fringes, taking into account the phase shifts $\Delta\varphi_n(x,y)$

$$A(x,y) = abs\left(\sum_{n=1}^{N} I_n(x,y)\exp[i\Delta\phi_n(x,y)\right) \tag{3}$$

and

$$\phi(x,y) = \arg\left(\sum_{n=1}^{N} I_n(x,y)\exp[i\Delta\phi_n(x,y)\right). \tag{4}$$

Different approaches towards the appropriate number of phase steps or towards the influence of non-equally spaced phase shifts on the demodulation accuracy are reported in literature [32].

For four shifted images with phase distances of $\pi/2$ the demodulation equations are simplified to simple trigonometric relations, for higher frame numbers averaging effects can be exploited for accuracy. Nevertheless, it should be mentioned that for monitoring dynamic processes, the ideal is to reduce the frame number to one frame (or in practise to two frames). With a dual shot imaging setup, two π–shifted frames can be obtained in a sequential way, whereas in single shot configurations a two channel pathway is assembled, exploiting polarization or diffraction effects, and a phase shift of π between the two spatially separated frames is introduced.

By building the difference image between the two frames the background term $B(x,y)$ can be reduced. This background-free difference image can now be demodulated with respect to amplitude or phase by so-called single frame processing methods [33].

These methods are based on analytic signal theory. In particular, the 2D analytic approach [34] and the monogenic approach [35] should be mentioned for single frame demodulation. In the 2D analytic approach amplitude and phase map can be expressed as

$$A(x,y) = \sqrt{f^2(x,y) + H_x{}^2 f(x,y) + H_y{}^2 f(x,y) + H_T{}^2 f(x,y)} \tag{5}$$

$$\phi(x,y) = \operatorname{atan}\left(\frac{\sqrt{H_x{}^2 f(x,y) + H_y{}^2 f(x,y) + H_T{}^2 f(x,y)}}{f(x,y)} \right), \tag{6}$$

where H_x, $H_{y,}$ and H_T represent the partial and total Hilbert transform [36] applied to the difference image f(x,y).

A two frame demodulation scheme is based on the monogenic signal approach [37, 38] with amplitude and phase map expressed as

$$A(x,y) = \sqrt{f^2(x,y) + R_x{}^2 f(x,y) + R_y{}^2 f(x,y)} \tag{7}$$

$$\phi(x,y) = \operatorname{atan}\left(\frac{\sqrt{R_x{}^2 f(x,y) + R_y{}^2 f(x,y)}}{f(x,y)} \right), \tag{8}$$

where R_x and R_y represent the two components of the Riesz transform given as

$$R_x = \frac{x}{2\pi r^3} \otimes (.) = \frac{\cos\vartheta}{2\pi r^2} \otimes (.) \quad \text{and} \quad R_y = \frac{y}{2\pi r^3} \otimes (.) = \frac{\sin\vartheta}{2\pi r^2} \otimes (.),$$

where $\otimes$ (.) denotes the convolution applied on the image $f(x,y)$, and (r, ϑ) the polar coordinates of radius and angle. Furthermore, by the ratio of both Riesz components the orientation of fringes or structures can be determined. This approach is to be preferred in case of aiming at a more isotropic response of the demodulation scheme, as briefly illustrated in Figure 2.

http://dx.doi.org/10.5772/53509

The development of these single shot methods is an on-going process, especially in the case of exploiting the potential of FF-OCM for dynamic scenes. Alternative approaches use micro-mirror devices [39] instead of conventional optical components, such as a Wollaston prism for a partial beam shifting [40].

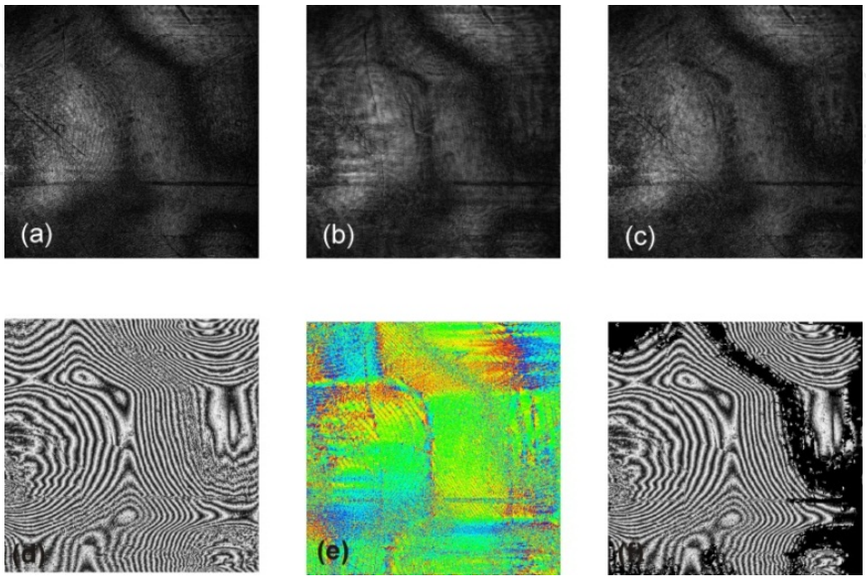

Figure 2. Comparison of demodulation schemes: (a-c) demodulated amplitude map applying (a) phase stepping, (b) 2D analytic signal approach, (c) monogenic signal approach as demodulation methods, (d) and (e) phase and fringe orientation map applying the monogenic approach, and (f) phase map with a superimposed reliability mask (based on the amplitude map for confidence estimation). The good match between the phase stepping approach (a) (assumed as ground truth) and the both single frame approaches (b) and (c) can be seen.

4. FF-OCM for technical material imaging

In the last decade, OCT imaging has been established as non-destructive method for investigating technical structures and processes. It partly benefited from the continuous improvement and perfection of OCT technique in numerous applications in the field of medicine. This newly gained knowledge was also transferred into the field of material research. In particular, functional OCT extension techniques such as PS-OCT, DPC-OCT, elastography-OCT [41, 42], or Doppler OCT have been introduced into the evaluation of technical sample structures and related material properties and features.

In the field of FF-OCM, a similar development from medical and biological applications to technical applications can also be observed. Typical samples, which may be probed by FF-OCM, are found in polymer materials as multilayer or filler enriched polymer foils, where the subsequent layers and filler particles can be visualized, (Figure 3a, b); fiber-reinforced materials of different type of manufacturing, (Figure 3c, d), or semi-transparent minerals, (Figure 3e, f). The quality assessment of organic coatings for a consistent material protection should be named as a further interesting application field of FF-OCM.

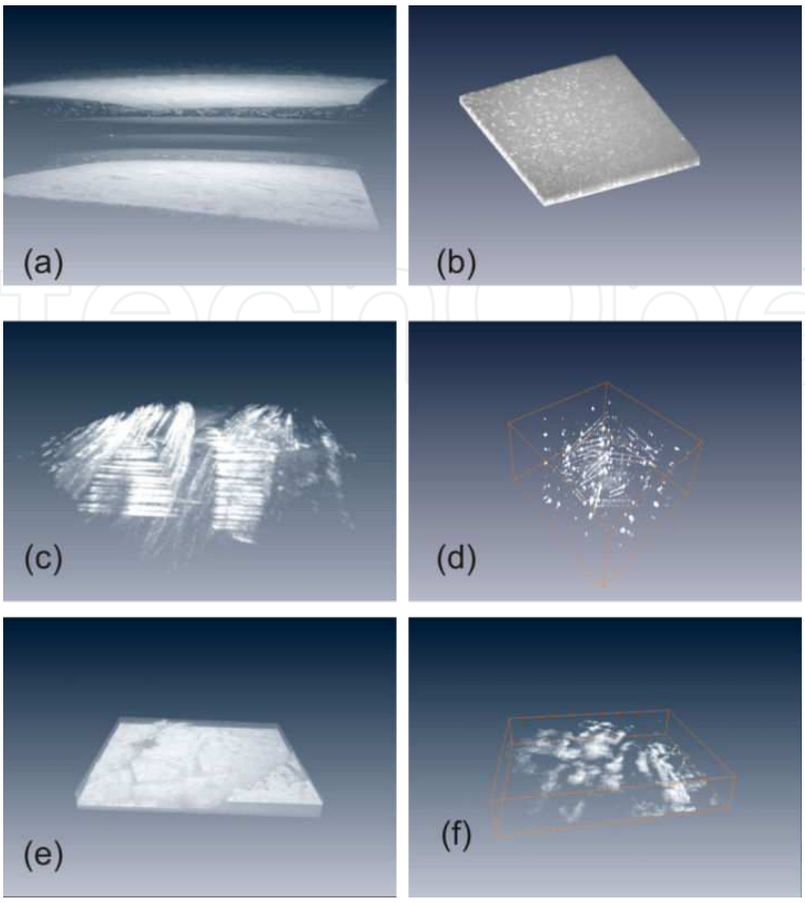

Figure 3. Examples of technical specimens investigated by FF-OCM: 3D volume rendering of a (a) multilayer foil and (b) functional polymer foil containing metallic micro-particles, (c) and (d) inside of a fiber-reinforced polymer sample with casted woven fibers in epoxy-resin (c) and with extruded short glass fibers in polypropylene (d) as filler materials, (e) Halit mineral specimen (finding place: Bolivia) with (f) included defect structures. The imaging volume yields depending on the sample ~ 1x1x0.2...0.4 mm^3.

In the next section, we consider in detail the abilities of FF-OCM to explore fiber-reinforced polymers or polymer materials under stress, which often have been imaged also by conventional OCT. We further consider the potential of different polarization sensitive OCT and OCM versions.

4.1. FF-OCM for characterization of fiber–reinforced polymers

Fiber reinforced polymers play an important role in the design of novel materials with specific and tuneable properties. The characterization of the internal fiber distributions within the matrix material can provide insights into material features or highlight potentials for improving the manufacturing process. Fiber structures differ with respect to their fiber concentration, with respect to the different manufacturing conditions (e.g. woven or randomly aligned fibers), or with respect to their functional role as filler components in materials.

http://dx.doi.org/10.5772/53509

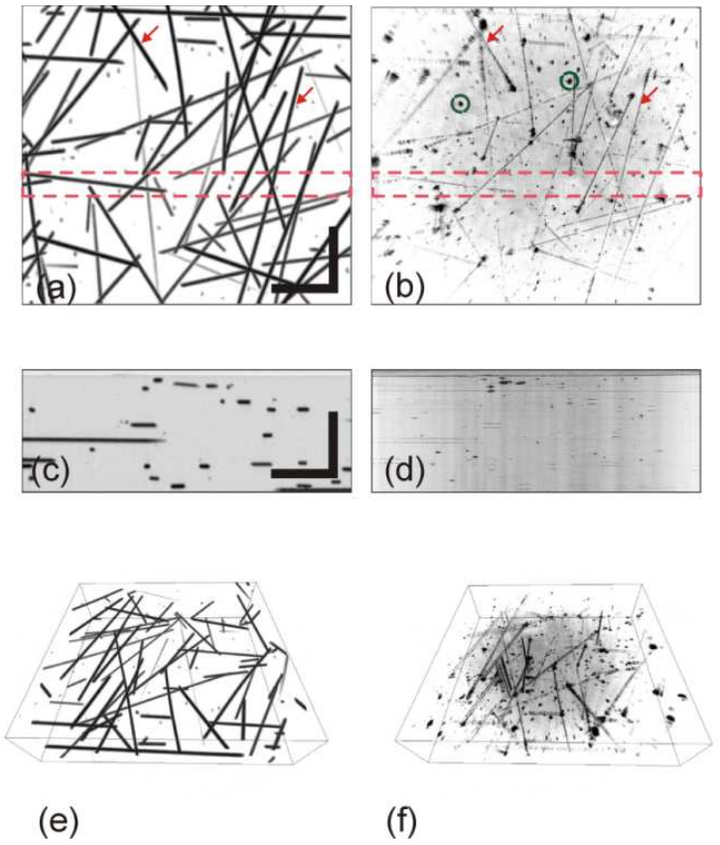

Figure 4. Comparison of the visualization characteristics between micro-CT and FF-OCM: Corresponding sites of the SGF-PP sample probed by micro-CT (left) and by FF-OCM (right), depicted as horizontal (top), cross-sectional (middle) and 3D view (bottom). Reprinted from [31], with permission from Elsevier, © 2012.

Often micro-CT is the method of choice for analyzing these polymer samples. In [31] polymer sheets of polypropylene (PP) containing short glass-fiber (SGF) as fillers are investigated applying both techniques, CT and FF-OCM, to compare and add their partly complementary imaging abilities for the visualization of inclusions or defects. Figure 4 shows a 3D image stack of a SGF-PP composite recorded with either technique. Note the good match between both techniques with respect to fiber localization and detection. Furthermore, complimentary information can be extracted through CT and OCM: the total volume of the fiber is visible in the CT reconstruction; in FF-OCM reconstruction, the reflection signal at front- and backside of the fibers are visible, and we can recognize various crystallization artefacts and micro-cracks there. Due to the low X-ray absorption difference these artefacts are not visible in CT imaging.

After probing, the recorded data can be improved by image processing. Mathematical image enhancement, for example, allows to reduce noise and illumination effects or to adjust the contrast [43]. The application of a background correction based on a morphological filtering for the SGF-PP sample is illustrated in Figure 5.

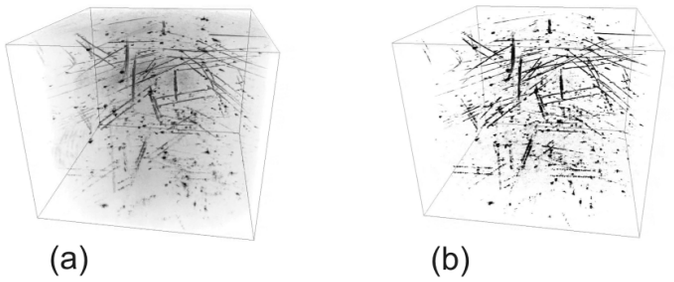

Figure 5. volume rendering of a SGF-PP compound: (a) original FF-OCM image stack, (b) enhanced structures after morphological background correction and noise filtering. The imaging volume yields ~ 1x1x0.3 mm^3. Reprinted from [31], with permission from Elsevier, © 2012.

A subsequent wavelet and shearlet based filtering and optimization approach [44] can separate the detected and pre-processed structures (Figure 6a) into fibers and spherical artefacts or cracks. This is done in a mathematical way, (Figure 6b and c).

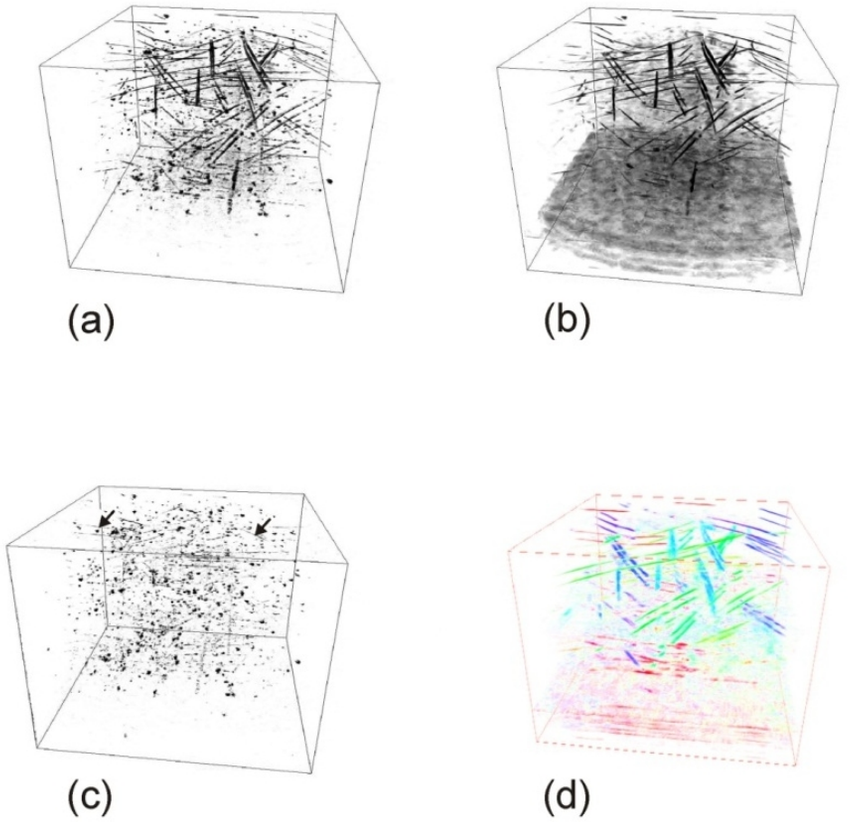

Figure 6. Illustration of the object separation, based mathematically on a shearlet and wavelet approach: the complete pre-processed 3D image stack (SFGF-PP sample) (a) and mathematically separated 3D stacks, containing fibers (b) and crystallization defects (c) as components. The local orientation of fibers (d), extracted by a monogenic signal approach, is represented in a colour encoded version. Reprinted from: [31], with permission from Elsevier, © 2012.

http://dx.doi.org/10.5772/53509

Finally, we can determine the local orientation of the fibers by means of a monogenic (complex-valued) signal approach, as can be seen in Figure 6d. For the orientation estimation, the MonogenicJ toolbox of EPFL has been used [45].

4.2. FF-OCM for monitoring strained /stressed polymers

The previous fiber-composite application is related to a static imaging and analysis of the polymer sample. Now we discuss the ability of FF-OCM to monitor dynamic scenes, e.g. polymers under load in a tensile testing. In [46] we have already reported a similar example: There, a rubber particle filled PP polymer under load was investigated in a tensile testing unit by spectral domain OCT. A local polymer region showing necking and flowing behaviour versus a static region could be distinguished after reaching the yield point. By calculating the speckle variance map over a temporal sequence of OCT reflectivity images, the static and dynamic region could be visually enhanced and the front of material flow could be identified (Figure 7).

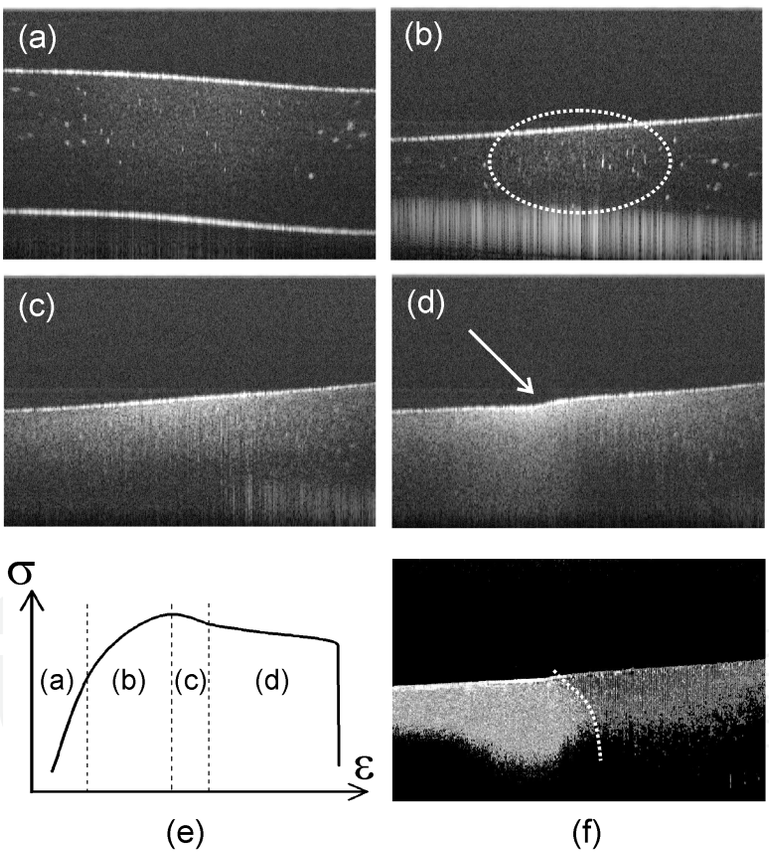

Figure 7. Dynamic stretching process monitored by SD-OCT: (a)-(d) single-frame reflectivity scans (cross sectional views) by OCT imaging showing a rubber particle filled PP polymer test bar (thickness: 1mm) under increasing tensile load, observed at different times. (e) Simultaneously measured strain-stress curve, indicating different regions which correspond to the sample stages (a)-(d): (a) linear elastic region, (b) non-linear elastic region and beginning of plastic deformation leading to increased scattering, (c) permanent plastic deformation after crossing the yield point and onset of necking, (d) pronounced necking (necking front indicated with arrow), finally leading to fracture. (f) Statistical evaluation (speckle variance map) of cross-sections taken between regimes (c) and (d) to visualize front of material flow during necking, as indicated by dotted line. Reprinted from [46], with permission from OSA, ©2010.

A similar experiment was repeated during FF-OCM measurements [47]. A tensile test unit was included in the sample arm of the interferometric FF-OCM setup, and the focus of the imaging was fixed at a defined depth position of interest. Again, the sample consists of a thin SGF-PP polymer sheet. We could also verify a (horizontal) flowing behaviour of the polymer matrix along the extending fracture in the material by the FF-OCM imaging technique as well. In addition, the normalized variance (second moment) and skewness (third moment) maps are computed over a temporal sequence of reflectivity images, (Figure 8). Furthermore, we also monitored the jumping up and final breaking of fibers within the polymer.

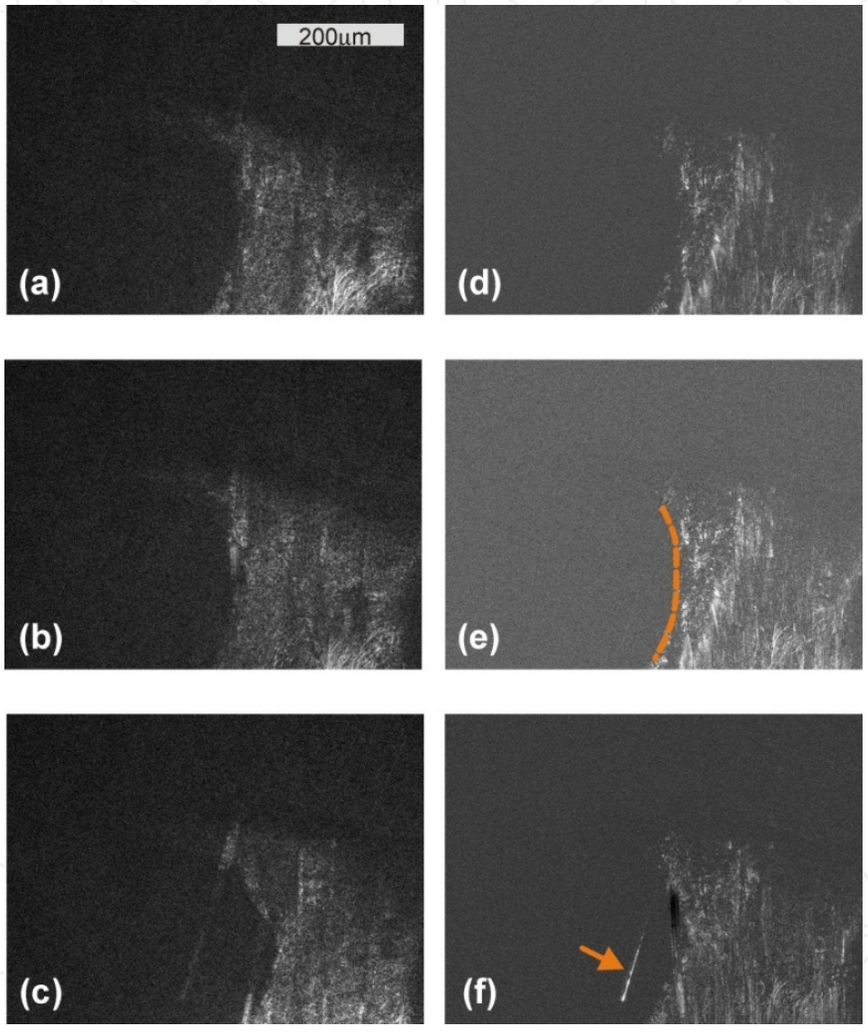

Figure 8. Dynamic tensile test imaging: (a)-(c): single-frame reflectivity scans (horizontal en-face views) by FF-OCM imaging, showing a glass fiber-reinforced polymer test sample under increasing tensile load, observed at different times. Statistical evaluation: (d) normalized variance map, (e) and (f) skewness map at the beginning and at a later point in time (computed over a temporal sequence of reflectivity scans). The front of material flow/fracture line is indicated by the dashed line, the arrow indicates a fiber leaping up.

To visualize dynamic processes without motion artefacts, a sufficient frame rate is required which matches the process dynamics. To guarantee high speed imaging in FF-OCM, on the one hand a suitable demodulation approach (see Section 3) has to be applied, and on the other

http://dx.doi.org/10.5772/53509

hand a fast enough detection system has to be chosen. Alternatively to the CCD camera used in static FF-OCM imaging applications, we recently applied a scientific CMOS (sCMOS) camera [47] for dynamic imaging. This enables us to obtain a frame rate that is sufficiently fast compared to CCD, that still has an acceptable sensitivity (70 dB with 4 x 4 binning) and is combined with an almost linear response over the 16-bit imaging range.

4.3. PS-FF-OCM imaging

Polarization sensitive (PS) versions of OCT allow us to obtain functional information from the material: its optical anisotropies and birefringence properties. As in the case of polymers, conclusions can be drawn about internal stress or strain fields in the PS probed sample: The strain fields can be explained e.g. by stress induced during the solidification or extrusion process. A reorientation of polymer molecular chains to a preferred linear alignment under stretching conditions or an already inherent orientational birefringence may cause the optically anisotropic behaviour of polymer material. The temporal evolution of such stress states caused by dynamic processes such as loading, stretching, extrusion, crystallization, or heating can be suitably monitored by PS-OCT.

A PS-OCT imaging can be accomplished by extending a conventional OCT setup with additional polarization optical components (i.e. polarizer, wave plates, and polarizing beam splitters) as illustrated schematically in Figure 9. Dual channel detection with respect to both orthogonal polarization directions can now be performed. In addition to the intensity-based reflectivity, further phase retardation and optical axis orientation can be determined. Using Stokes vector formalism, also the degree of polarization uniformity (DOPU) or birefringence (as change of retardation over depth) can be examined [48].

Conventional FF-OCM may be extended as well to a polarization sensitive FF-OCM version (PS-FF-OCM) [49]. The extension is realized similar to the time domain PS-OCT configuration described above. Here, either two cameras are applied using a conventional polarizing beamsplitter, or the images are taken by a single camera with a Wollaston prism mounted at the front. The Wollaston prism splits the two orthogonally polarized image components which are recorded at a single CCD area detector. It should be mentioned that a very good adjustment of the camera system or a pixel-to-pixel registration between the two image components is necessary to reduce artefacts of slightly differing alignments.

As interesting specimens for material scientists, strained or stressed polymer samples were inspected. In Figure 10, a polymer sheet exhibiting known external or internal defects is shown, examined by PS-OCT during a stretching process. In the intensity-based OCT image, defects are slightly recognizable, but the fringe pattern in the retardation image point to defects through the deviations from the regular pattern. By applying increasing stress, the evolution of the fringes can be observed over time. The progression of fringe frequency over imaging depth or time correlates with the formation of internal stress and strain fields.

Through subsequent image processing and under consideration of optical material constants, a quantitative analysis of strain based on the retardation fringe pattern can be performed [50].

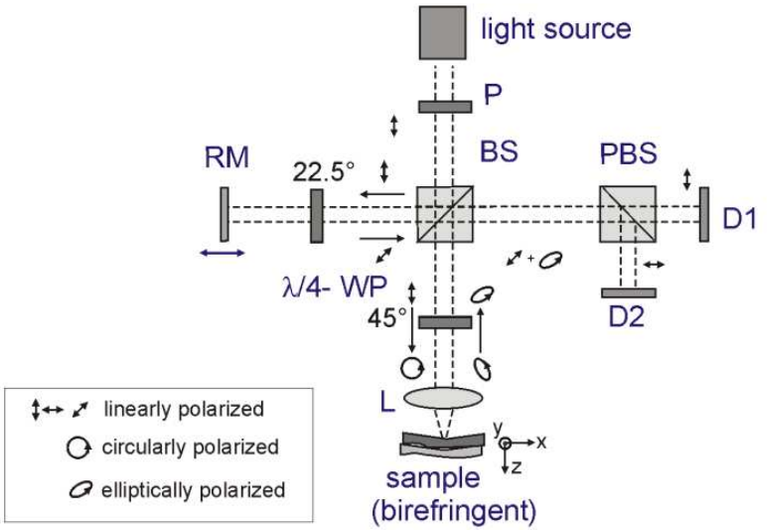

Figure 9. The optical (time domain) PS-OCT setup (Michelson configuration) containing additionally polarizing optical elements (WP: wave plate, P: polarizer, PBS: polarizing beam splitter) for a dual channel detection (D1, D2).

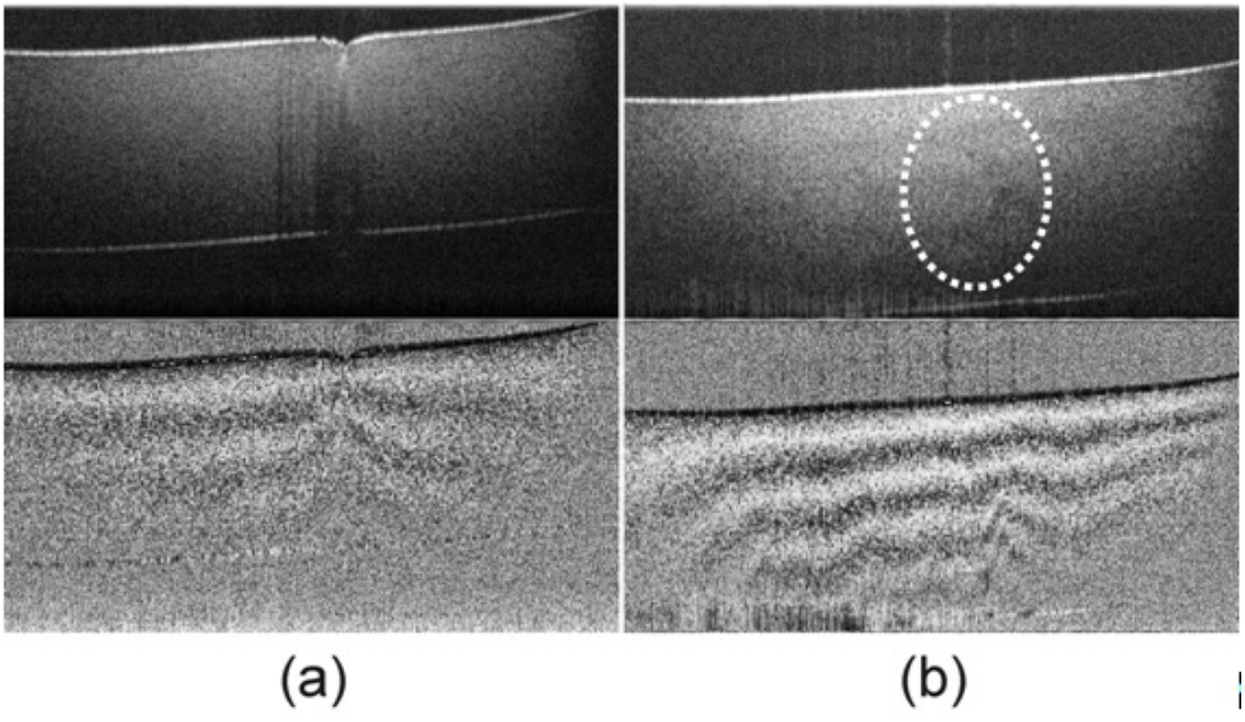

Figure 10. Strained polymer sample (thickness 1mm) under increasing tensile load under PS-OCT imaging shown as intensity cross-sections (upper images) and corresponding gray-scale encoded retardation images (bottom images): (a) sample exhibiting a surface defect, (b) sample with internal defect (visible as slightly darker, bow-shaped feature within marked region). Reprinted from [46], with permission from OSA, © 2010.

Another interesting example of PS imaging concerns the investigation of micro-structured polymer materials [51], represented here by a semi-transparent polymer mould for micromechanical wheels, to gain insight into hidden stress states resulting from the manufacturing and

http://dx.doi.org/10.5772/53509

from the subsequent curing processes. In Figure 11, the en-face reflectivity and retardation image of the micro-component is shown, which was probed under a transversal scanning scheme by means of PS-OCT imaging.

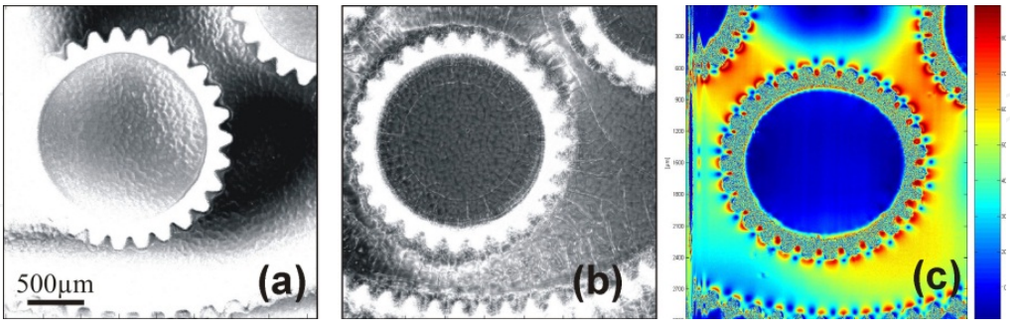

Figure 11. Micro-structured polymer part (photoresist mould for a micromechanical wheel, thickness 1.5 mm) imaged by PS-OCT [51]. The intensity-based reflectivity images are shown at surface (a) and backside (b), and the corresponding retardation image (c). Larger areas of regions with induced strain fields are visible between the wheels; smaller stressed regions appear between the teeth.

A similar region imaged by PS-FF-OCM is depicted in Figure 12. For the FF-OCM, an increased scattering in the polymer part is remarkable compared to OCT, (illumination: SLD).

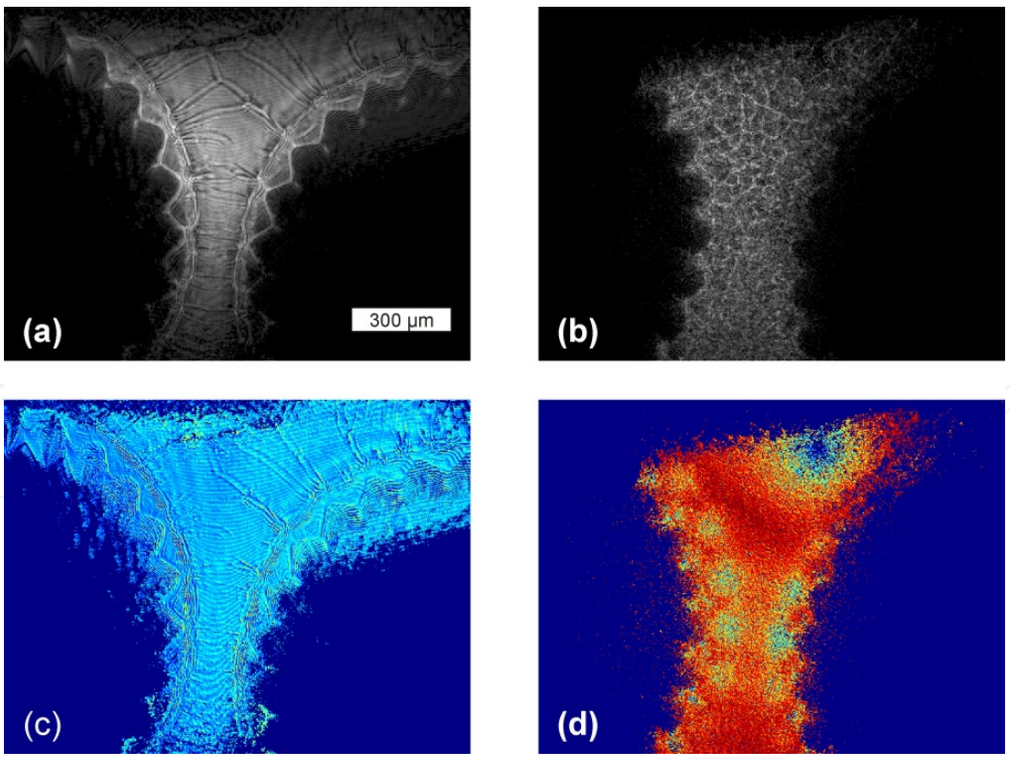

Figure 12. Micro-structured polymer part (section of photoresist mould) imaged by PS-FF-OCM. The intensity-based reflectivity images at surface (a) and backside (b), and the corresponding retardation images (c) and (d). Note smaller regions with local stress-strain fields between the teeth (d).

As a further application for PS-OCT, we briefly mention the in-situ monitoring of crystallization processes during the extrusion, shearing, and solidification of the polymer material [52]. The growing of polymer micro-crystallites and the evolution of different planar polymer structures during the processes can be visualized by PS-OCT and be analyzed with respect to the process parameters (temperature, pressure, speed). The resulting micro-crystalline structures within the polymer matrix are monitored by (PS)-FF-OCM imaging with a higher lateral resolution (compared to PS-OCT) as depicted in Figure 13. The different edges of the crystallite are clearly visible in the intensity-based full-field images. Furthermore, an optical anisotropy of the crystallites can be observed in the retardation images of the polarization sensitive full-field version.

Other PS-OCT or PS-FF-OCM imaging applications in a technical context concern ceramics [53], fiber-reinforced polymer compounds [54], or organic coatings [55]. However, without doubt the main application field for PS-OCT and PS-FF-OCM is still that of numerous medical applications. [56, 57].

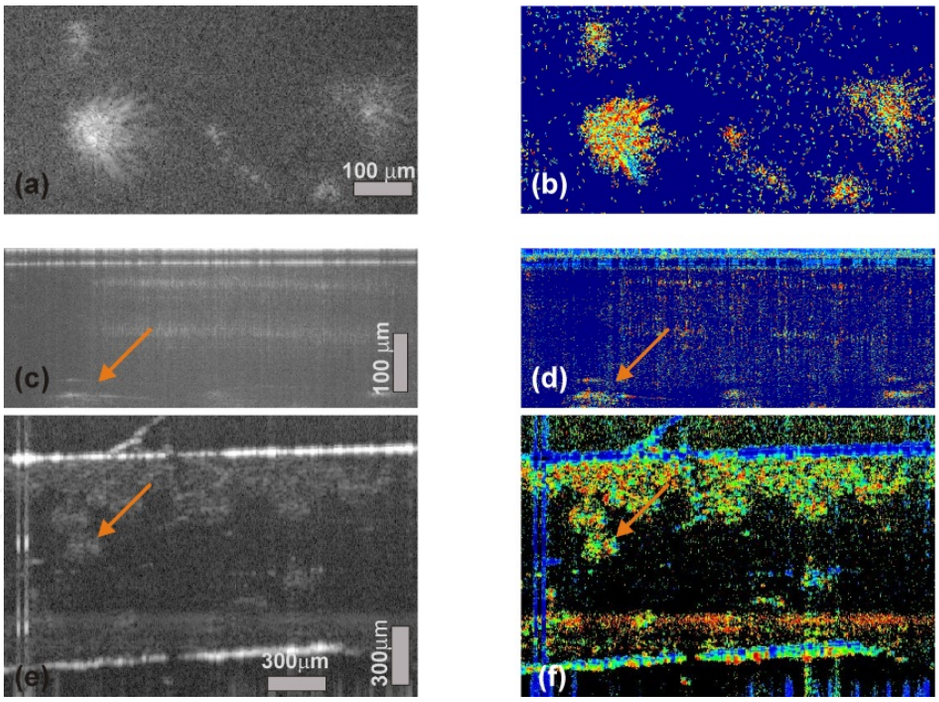

Figure 13. Visualization of micro-crystalline structures in isotactic polypropylene grown during the extrusion and crystallization process. (a) and (c) reflectivity images, (b) and (d) retardation images obtained by PS-FF-OCM. The images are depicted as en-face image (upper row) and as cross-section (middle row). For comparison: reflectivity (e) and retardation cross-sectional scans (f) of the entire polymer sample, examined by PS-OCT imaging. The arrows indicate micro-crystallites in both cross-sectional images (PS-FF-OCM and PS-OCT). Note the different fields of view in OCT and FF-OCM imaging.

http://dx.doi.org/10.5772/53509

4.4. Contrast modification in FF-OCM imaging

Additional to the issues of obtaining suitable resolution and focus depth in microscopy imaging, an appropriate contrast enhancement or modification is essential to emphasis special features of the specimen. Similar to configurations in microscopy, in FF-OCM different contrast modifications can be realized. Based on the traditional principle of Fourier plane filtering, a Fourier filter unit is incorporated into the FF-OCM setup, preferably as a Mach-Zehnder configuration. The Fourier filter unit comprehends a 4f configuration, depicted schematically in Figure 14. The key element is the optical Fourier filter in the back-focal plane of the entrance lens. Whereas in the past, the optical filter was often manufactured as a silica or glass component, the filter can nowadays be realized by a spatial light modulator (SLM) [58].

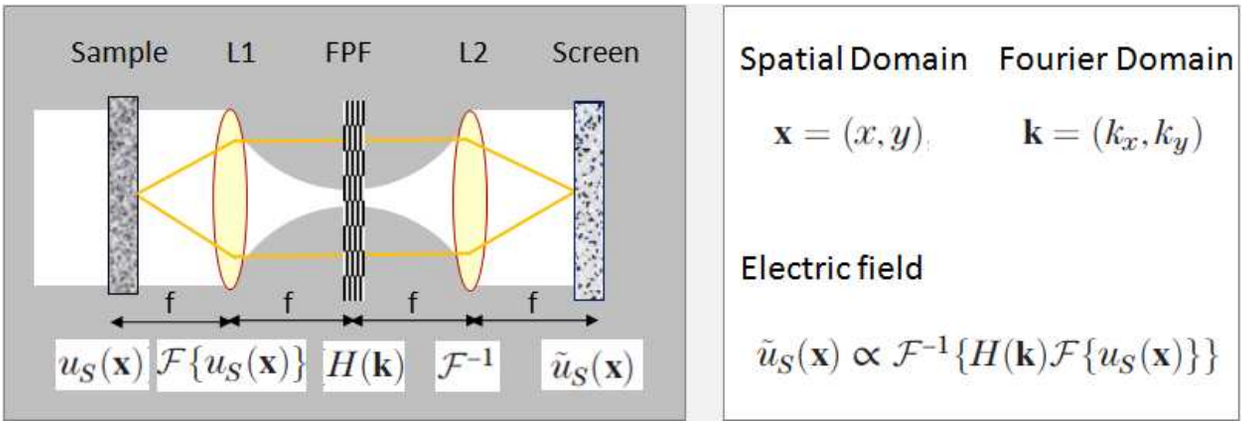

Figure 14. Illustration scheme of the optical Fourier filtering principle. The 4f-configuration is depicted in the left panel. It consists of the sample, entrance lens (L1), Fourier filter (FPF), exit lens (L2), and reconstructed object recorded at the screen. Each component is positioned at a distance to the focal length f from one another. The mathematical terms are given in the right panel: forward and inverse Fourier transform (F and F^{-1}) and filter function $H(k)$ applied to sample wave function $u_s(x)$ results in a modified wave field $\tilde{u}_s(x)$.

The SLM, as a pixelated liquid crystal array, is addressable with different amplitude or phase filter functions. The contrast can now be changed flexibly and be adapted to the sample [59]. Similar to microscopy, phase contrast, Schlieren contrast, or spiral phase contrast are emulated to enhance partial sites of the imaged structure (Figure 15). But in contrast to microscopy imaging, the contrast modification in FF-OCM can now be performed in a depth-resolved way (Figure 16).

Fourier plane filters In FF-OCM are most useful for imaging stratified or layered, almost transparent samples like varnish coatings or droplets. It should be mentioned that for highly scattering materials, phase-based Fourier filtering may fail because no fixed phase relation can be build up between the random scatters. Here, a novel method for focusing light through scattering materials seems a promising approach [60, 61].

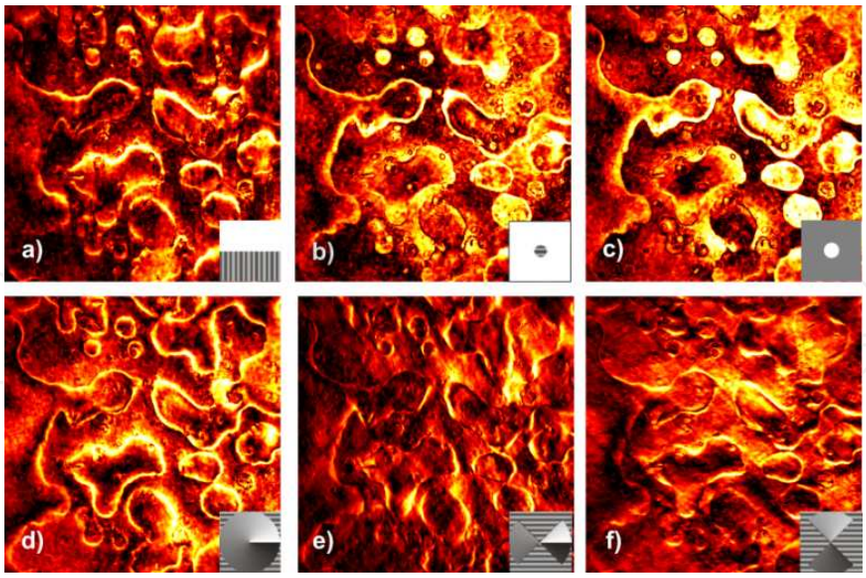

Figure 15. Illustration of flexible contrast in FF-OCM imaging on a test sample (organic varnish droplets applied to both the front and back surface of a glass slide, mimicking a multilayered technical structure). The emulated contrast comprehends (a) dark field contrast, (b) Schlieren contrast, (c) phase contrast, (d) isotropic spiral-phase contrast, and (e), (f) anisotropic contrast with cone-like spiral phase filters. A pseudo-colour representation is chosen. The applied FPFs are indicated schematically in the insets. Reprinted from [59], with permission from GIT Verlag.

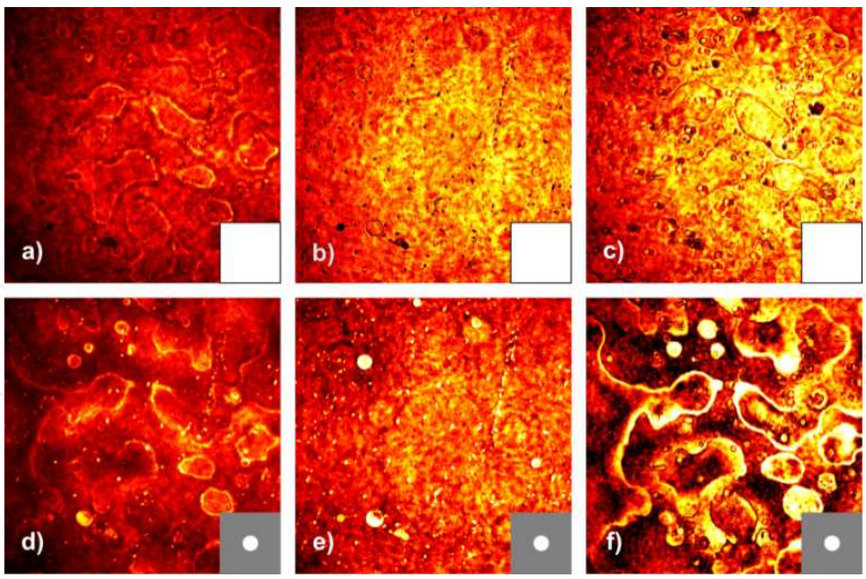

Figure 16. Comparison of depth-selective contrast modification in microscopic and FF-OCM imaging, exemplified for a varnish droplet test sample. The features are visualized in (a) and (d) by conventional microscopy, in (b), (c), (e), and (f) by OCM imaging; the scans are taken at the upper ((b) and (e)), and lower interface ((c) and (f)) of the test sample. First row: bright field mode; second row: phase contrast mode. Reprinted from [59], with permission from GIT Verlag.

http://dx.doi.org/10.5772/53509

5. Conclusions and outlook

We have demonstrated different applications of FF-OCM in the field of material sciences, with a particular focus on examples from polymer sciences. FF-OCM is a promising non-destructive technique for the investigation of novel polymer materials, in particular if local distribution of fibers and filler particles should be monitored or combined with polarization-sensitive versions if local stress states are of interest. Furthermore, we have illustrated how adapted image processing can further contribute to a better extraction of the information contained in OCT and OCM images. It should be mentioned that in diverse applications, OCT and FF-OCM measurements may supplement each other by providing partly complementary information due to their different resolution and penetration abilities.

Although literature about OCT and FF-OCM applications in material research is in the minority compared to applications in the medical field, we hope that newly established dialogue between these two research areas and the increase of interest on the side of material scientists to take up novel techniques may continue into future.

Acknowledgements

The financial support by the Federal Ministry of Economy, Family and Youth, the National Foundation for Research, Technology and Development is gratefully acknowledged. For the micro-CT measurements on SGF-PP samples, we thank Dietmar Salaberger and Bernhard Plank at the Applied University of Upper Austria, Wels. Furthermore, we are grateful to Prof. Heide at the TU Bergakademie Freiberg for providing the mineral specimens, Peter Hierzenberger and Roman Rittberger at Polymer Sciences Department, JKU Linz for preparing the different polymer materials. We acknowledge Prof. Ritsch-Marte and team at the Medical University Innsbruck for continuous support in SLM techniques. Jean-Luc Bouchot at JKU Linz and Sören Häuser at the University Kaiserslautern are given thanks for their contributions in image processing.

Author details

Bettina Heise[1,2*], Stefan Schausberger[1] and David Stifter[1]

*Address all correspondence to: Bettina.Heise@jku.at

1 Christian Doppler Laboratory for Microscopic and Spectroscopic Material Characterization, Johannes Kepler University, Linz, Austria

2 FLLL, Johannes Kepler University, Linz, Austria

References

[1] Harrer B, Kastner J. X-ray microtomography: Characterization of structures and defect analysis, In: Fabrication and Characterization in the Micro-Nano Range, A. Lasagni, F. Lasagni (Publ.), Vol 10, Springer Verlag, Heidelberg, 2011. p119-149. doi 10.1007/978-3-642-17782-8.

[2] Huang D, Swanson EA, Lin CP, Schuman JS, Stinson WG, Chang W, Hee MR, Flotte T, Gregory K, Puliafito CA, Fujimo JG. Optical Coherence Tomography, Science 1991; 254 (5035), 1178–1181.

[3] Fercher AF, Sander B, Jorgensen TM, Andersen PE. Optical Coherence Tomography. Encyclopedia of Analytic Chemistry 2009.

[4] Li N, Zhang S, Hou J, Jang IK, Yu B. Assessment of Pulmonary Artery Morphology by Optical Coherence Tomography. Heart Lung Circ. 2012; in press, online August 2012.

[5] Payton S. Kidney cancer: First in vivo study shows optical imaging can distinguish renal cancer from normal tissue. Nat. Rev. Urol. 2012; 9(6), 294.

[6] Shlivko IL, Petrova GA, Zorkina MV, Tchekalkina OE, Firsova MS, Ellinsky DO, Agrba PD, Kamensky VA, Donchenko EV. Complex assessment of age-specific morphofunctional features of skin of different anatomic localizations. Skin Research and Technology, in press, online June 2012.

[7] Park HC, Song C, Kang M, Jeong Y, Jeong KH. Forward imaging OCT endoscopic catheter based on MEMS lens scanning, Opt. Lett. 2012; 37(13), 2673-2675

[8] Davidson M, Kaufmann K, Mazor I, Cohen F. An application of interference microscopy to integrated circuit inspection and metrology. SPIE 1987; Proc. 775, 233-241.

[9] Liang H, Lawman S. High precision dynamic multi-interface profilometry with optical coherence tomography. Appl. Optics 2011; 50(32), 6039-6048.

[10] Yang ML, Winkler AM, Klein J, Wall A, Barton JK. Using Optical Coherence Tomography to Characterize the Crack Morphology of Ceramic Glaze and Jade. In: Selected Topics in Optical Coherence Tomography. Intech, online: doi: 10.5772/31213.

[11] Prykäri T, Czajkowski J, Alarousu E, Myllylä R. Optical coherence tomography as an accurate inspection and quality evaluation technique in paper industry. Opt. Rev. 2010; 17(3), 218-222.

[12] Webster PJL, Yu JXZ, Leung BYC, Anderson MD, Yang VXD, Fraser JM. In situ 24 kHz coherent imaging of morphology change in laser percussion drilling. Opt. Lett. 2010; 35(5), 646-648.

[13] Stifter D. Beyond biomedicine: a review of alternative applications and developments for optical coherence tomography. Appl. Phys. 2007; 88, 337-479.

[14] Xi C, Marks DL, Parikh DS, Raskin L, Boppart SA. Structural and functional imaging of 3D microfluidic mixers using optical coherence tomography. PNAS 2004; 101(20), 7516-7521.

[15] Stifter D, Burgholzer P, Höglinger O, Götzinger E, Hitzenberger CK. Polarisation-sensitive optical coherence tomography for material characterisation and strain-field mapping. Appl. Phys. A 2003; 76(6), 947-951.

[16] Wieser W, Biedermann BR, Klein T, Eigenwillig CM, Huber R. Multi-Mega-hertz OCT: High quality 3D imaging at 20 million A-scans and 4.5 GVoxels per second. Opt.Express 2010; 18(14), 14685-14704.

[17] Sun J, Xie H. MEMS-Based Endoscopic Optical Coherence Tomography. Inter. J. Optics 2011; ID 825629, online: doi:10.1155/2011/825629.

[18] Ju MJ, Lee SJ, Kim Y, Shin SG, Kim HY, Lim Y, Yasuno Y, Lee BH. Multimodal analysis of pearls and pearl treatments by using optical coherence tomography and fluorescence spectroscopy. Opt. Express 2011; 19(7), 6420-6432.

[19] Skala MC, Fontanella A, Hendargo H, Dewhirst MW, Izatt, JA, Combined Hyperspectral and Spectral Domain Optical Coherence Tomography Microscope for Non-invasive Hemodynamic Imaging. Opt. Lett. 2009; 34(3), 289-291.

[20] Liu G, Chen Z. Fiber-based combined optical coherence and multiphoton endomicroscopy. J Biomed Opt. 2011, 16(3), 036010-1-4.

[21] Graf BW. Multimodal in vivo skin imaging with integrated optical coherence and multiphoton microscopy. IEEE J. Selected Topics in Quantum Electronics 2012; 18(4), 1280-1286.

[22] Dubois A, Vabre L, Boccara AC, Beaurepaire E. High-Resolution Full-Field Optical Coherence Tomography with a Linnik Microscope. Appl. Opt. 2002; 41(4), 805-812.

[23] Fang L, Li S, Nie Q, Izatt JA, Toth CA, Farsiu S. Sparsity Based Denoising of Spectral Domain Optical Coherence Tomography Images. Biomed. Opt. Express, 3(5), 927-942.

[24] Huang Y, Liu X, Kang JU. Real-time 3D and 4D Fourier domain Doppler optical coherence tomography based on dual graphics processing units. Biomed. Opt. Express 2012; 13(9), 2162-2174.

[25] Dubois A, Boccara AC. Full-Field Optical Coherence Tomography. In: Drexler W, Fujimoto JF (eds.) Optical Coherence Tomography. Springer; 2008. p565-591.

[26] Bayleyegn MD, Makhlouf H, Crotti C, Plamann K, Dubois A, Ultrahigh resolution spectral-domain optical coherence tomography at 1.3 μm using a broadband superluminescent diode light source. Opt. Commun. 2012, in press, online August 2012, dx.doi.org/10.1016/j.optcom.2012.07.066.

[27] Wiesauer K. Pircher M, Götzinger E, Bauer S, Engelke R, Ahrens G, Grützner G, Hitzenberger CK, Stifter D. En-face scanning optical coherence tomography with ultra-high resolution for material investigation. Opt. Express 2005; 13 (3), 1015-1024.

[28] Hartl I, Li XD, Chudoba C, Ghanta RK, Ko TH, Fujimoto JG, Ranka JK, Windeler RS. Ultrahigh-resolution optical coherence tomography using continuum generation in an air–silica microstructure optical fiber. Opt. Lett. 2001; 26, 608-610.

[29] Humbert G, Wadsworth WJ, Leon-Saval SG, Knight JC, Birks TA, Russell PSJ, Lederer MJ, Kopf D, Wiesauer K, Breuer EI, Stifter D. Supercontinuum generation system for optical coherence tomography based on tapered photonic crystal fibre. Opt. Express 2006; 14 (4), 1596-1603.

[30] Dubois A, Grieve K, Moneron G, Lecaque R, Vabre L, Boccara C. Ultrahigh- resolution full-field optical coherence tomography. Appl. Opt. 2004; 43, 2874–2883.

[31] Heise B, Schausberger SE, Häuser S, Plank B, Salaberger D, Leiss-Holzinger E, Stifter D. Full-Field Optical Coherence Microscopy with a Sub-nanosecond Supercontinuum Light Source for Material Research. Opt. Fiber Technol. 2012, in press, dx.doi.org/10.1016/j.yofte.2012.07.011.

[32] Adachi M. Phase-shift algorithm for white-light interferometry insensitive to a linear error in phase shift increment. 2005; Proc. SPIE 6048, 604806-1-9.

[33] Malacara D, Servin M, Malacara Z. Inteferogram Analysis for Optical Testing. CRC Press, Taylor& Francis Group (2005). p475-491.

[34] Hrebesh MS. Full-Field & Single-Shot Full-Field Optical Coherence Tomography: A novel technique for biomedical imaging applications. Advances in Optical Technologies 2012 (2012); ID 435408, online: doi:10.1155/2012/435408.

[35] Bernstein S, Bouchot, JL Reinhardt M, Heise B. Generalized Analytic Signals in Image Processing: Comparison, Theory and Applications. TIM Birkhäuser, accepted 2012.

[36] Hahn SL. Multi-dimensional complex signals with single-orthant spectra. Proc. IEEE 1992; 80, 1287-1300.

[37] Felsberg M, Sommer G. The monogenic signal. IEEE Trans. Sign. Proc. 2001; 49(12), 3136-3144.

[38] Larkin KG, Bone DJ, Oldfield MA. Natural demodulation of two-dimensional fringe patterns. I. General background of the spiral phase quadrature transform. J. Opt. Soc. Am. A 2001; 18(8), 1862-1870.

[39] Nugroho W, Hrebesh MS, Sato M. Simulation of basic characteristics of single-shot full-field optical coherence tomography using spatially phase-modulated reference light. Opt. Rev. 2011; 18(4), 343-350.

[40] Hrebesh MS, Dabu R, Sato M. In vivo imaging of dynamic biological specimen by real-time single-shot full-field optical coherence tomography. Opt. Commun. 2009; 282, 674-683.

[41] Razani M, Mariampillai A, Sun C, Luk TW, Yang VX, Kolios MC. Feasibility of optical coherence elastography measurements of shear wave propagation in homogeneous tissue equivalent phantoms. Biomed. Opt. Express 2012; 3(5), 972-980.

[42] Adie SG, Liang X, Kennedy BF, John R, Sampson DD, Boppart SA. Spectroscopic optical coherence elastography. Opt. Express 2010; 18(25), 25519-25534.

[43] Schlager V, Schausberger SE, Stifter D, Heise B. Coherence probe microscopy imaging and analysis for fiber-reinforced polymers. Springer LNCS 2011; 6688, 424-434.

[44] Häuser S. Fast Finite Shearlet Transform: a tutorial. Preprint University of Kaiserslautern, 2011, arXiv:1202.1773v1.

[45] Unser M, Sage D, Van De Ville D. Multiresolution monogenic signal analysis using the Riesz-Laplace wavelet transform, IEEE Trans. Image Proc. 2009; 18(11), 2402-2418.

[46] Stifter D, Leiss-Holzinger E, Major Z, Baumann B, Pircher M, Götzinger E, Hitzenberger CK, Heise B. Dynamic optical studies in materials testing with spectral-domain polarization-sensitive optical coherence tomography. Opt. Express 2010; 18(25), 25712-25725.

[47] Schausberger SE, Heise B, Bernstein S, Stifter D. Full-field optical coherence microscopy with a sCMOS detector for dynamic imaging, Opt. Lett., submitted.

[48] Baumann B, Baumann SO, Konegger T, Pircher M, Götzinger E, Schlanitz F. et al. Polarization sensitive optical coherence tomography of melanin provides intrinsic contrast based on depolarization. Biomed. Opt. Express 2012; 3(7), 1670-1683.

[49] Moneron G, Boccara AC, Dubois A. Polarization-sensitive full-field optical coherence tomography. Opt. Lett. 2007; 32(14), 2058-2060.

[50] Heise B, Wiesauer K, Götzinger E, Pircher M, Hitzenberger CK, Engelke R, Ahrens G, Grützner G, Stifter D. Spatially Resolved Stress Measurements in Materials with Polarisation-Sensitive Optical Coherence Tomography: Image Acquisition and Processing Aspects. J. Strain 2010; 46, 61-68.

[51] Wiesauer K, Pircher M, Götzinger E, Hitzenberger CK, Engelke R, Ahrens G, Grützner G, Stifter D. Transversal ultrahigh-resolution polarization-sensitive optical coherence tomography for strain mapping in materials. Opt. Express 2006; 14, 5945-5953.

[52] Hierzenberger P, Eder G, Heise B, Leiss-Holzinger E, Stifter D. In-situ monitoring of polymer crystallization by Optical Coherence Tomography (OCT). Proc. Advances in Polymer Science and Technology 2, Trauner Verlag, Linz 2011.

[53] Strakowski M, Pluciński J, Łoziński A, Kosmowski BB. Determination of local polarization properties of PLZT ceramics by PS-OCT. The European Physical Journal - Special Topics 2008; 154(1), 207-210.

[54] Wiesauer K, Pircher M, Götzinger E, Hitzenberger CK, Oster R, Stifter D. Investigation of glass–fibre reinforced polymers by polarisation-sensitive, ultra-high resolution optical coherence tomography: Internal structures, defects and stress. Composites Science and Technology 2007; 67(15-16), 3051–3058.

[55] Dubois A. Spectroscopic polarization-sensitive full-field optical coherence tomography. Opt. Express 2012; 20(9), 9962-9977.

[56] Kang H, Darling CL, Fried D. Nondestructive monitoring of the repair of enamel artificial lesions by an acidic remineralization model using polarization-sensitive optical coherence tomography. Dental Materials 2012; 28(5), 488-494.

[57] Baumann B, Pircher M, Götzinger E, Sattmann H, Wurm M, Stifter D, Schütze C, Ahlers C, Geitzenauer W, Schmidt-Erfurth U, Hitzenberger CK. Imaging the human retina in vivo with combined spectral-domain polarization-sensitive optical coherence tomography and scanning laser ophtalmoscopy. SPIE 2009; Proc. 7163; 71630N-1-6.

[58] Maurer C, Jesacher A, Bernet S, Ritsch-Marte M. What spatial light modulators can do for optical microscopy. Laser & Photonics Reviews 2011; 5(1), 81-101.

[59] Heise B, Schausberger SE, Stifter D. Coherence Probe Microscopy Contrast Modification and Image Enhancement. Imaging & Microscopy 2012; 2, 29-32.

[60] Vellekoop IM, Mosk AP. Focusing coherent light through opaque strongly scattering media.Opt. Lett. 2007; 32(16), 2309-2311.

[61] Stockbridge C, Lu Y, Moore J, Hoffman S, Paxman R, Toussaint K, Bifano T. Focusing through dynamic scattering media. Opt. Express 2012; 20(14), 15086-15092.